Ultra-thin epitaxial films of graphite and hexagonal boron nitride on solid surfaces

1997 J. Phys.: Condens. Matter 9 1

(http://iopscience.iop.org/0953-8984/9/1/004)

J. Phys.: Condens. Matter **9** (1997) 1–20. Printed in the UK PII: S0953-8984(97)64931-0

REVIEW ARTICLE

Ultra-thin epitaxial films of graphite and hexagonal boron nitride on solid surfaces

Chuhei Oshima†§ and Ayato Nagashima‡

† Department of Applied Physics, Waseda University, Okuobo 3-4-1, Shinjuku, Tokyo 169, Japan

‡ Department of Physics, Tokyo Institute of Technology, Ookayama 2-12-1, Meguro, Tokyo 152, Japan

Received 22 May 1996, in final form 7 August 1996

Abstract. In this article, we have reviewed the recent progress of the experimental studies on ultra-thin films of graphite and hexagonal boron nitride (h-BN) by using angle-resolved electron spectroscopy together with other techniques. The fundamental properties of these high-quality films are discussed on the basis of the data on dispersion relations of valence electrons, phonon dispersion etc. The interfacial orbital mixing of the π-state of the monolayer graphite (MG) with the d states of the reactive substrates is the origin for the phonon softening, expansion of the nearest-neighbour C–C distance, modification of the π-band, low work function, and two-dimensional plasmons with high electron density, etc. In the cases of weak mixing at the interface between the MG and relatively inert substrates, the observed properties of the MG are very close to the bulk ones. In contrast to the case for MG, the interfacial interaction between the h-BN monolayer and the substrate is weak.

Contents

1. Introduction

Graphite and hexagonal boron nitride (h-BN) are isostructural layered materials with strongly anisotropic chemical bonds [1]. In the basal plane of graphite (h-BN), as shown in figure 1,

§ Author to whom any correspondence should be addressed; e-mail: coshima@mn.waseda.ac.jp; fax: +81-35272-7507.

0953-8984/97/010001+20$19.50

carbon atoms (boron and nitrogen atoms) construct a two-dimensional (2D) honeycomb structure with strong covalent bonds, while the basal planes interact weakly with each other via Van der Waals bonds (with slightly ionic bonds). Therefore, graphite and h-BN exhibit strongly anisotropic character in many physical properties such as energy band structure, electrical conductivity, thermal conductivity, Debye temperature, phonon type, and magnetism type [2]. The strong anisotropic character appears also in their surface energies; the (0001) surface parallel to the basal plane has surface energy much lower than the other surfaces have. Consequently, the basal plane is preferentially grown on various solid surfaces. One basal plane can be supposed to be a big molecule in molecular crystals, which is sometimes called 'graphene'.

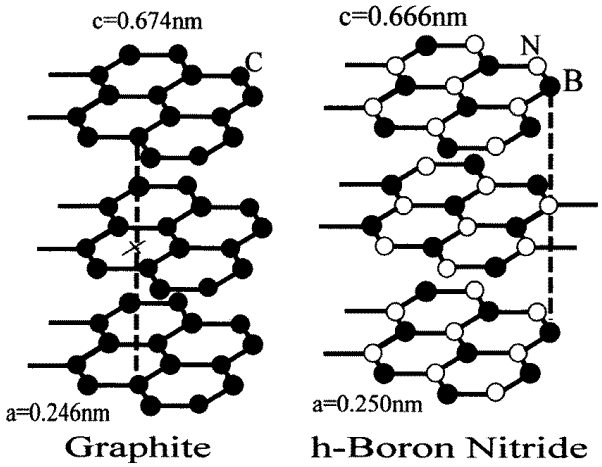

Figure 1. Schematic diagrams of crystal structures of graphite and h-BN.

On the other hand, the above-mentioned 2D bonds possess a high flexibility for bending of the basal plane; the transverse acoustic (TA) mode with a polarization perpendicular to the planes shows parabolic dispersion in a long-wavelength region [3], which is quite different from the linear dispersion in three-dimensional (3D) crystals [4]. In other words, the restoring force for mild bending of the basal plane is quite weak in comparison with that of 3D materials. In fact, 'nano-tubes' of graphite and h-BN constructed by rolling these basal planes were found and investigated by many authors [5, 6]. In another case, some ultra-fine particles and solids were found to be wrapped with bending graphite films [7].

In recent years, epitaxial films of these layered materials with only a few atomic layers have received a lot of attention, because of their peculiar characters. Thin films of graphite realized stable field-electron emission because of the extremely inert surface [8], and h-BN films grown on stainless steels reduced outgassing from a vacuum chamber [9] and also became an excellent barrier against hydrogen permeation [10]. In addition, thin films of graphite and h-BN weakly bonded to flat surfaces would be attractive in the field of fabrication of microelectronic devices such as tunnelling devices because of the spatially abrupt change of the electronic structure at the interface [11].

In this article, we review recent progress in experimental studies on fundamental properties of these thin films, which are investigated by angle-resolved electron spectroscopy, high-resolution electron energy-loss spectroscopy (HREELS) and ultraviolet photoelectron spectroscopy (UPS) together with x-ray photoemission spectroscopy (XPS),

low-energy electron diffraction (LEED), work-function measurement, and scanning tunnelling microscopy (STM). In addition, we report new data concerning the atomic structure of h-BN on a Ni(111) surface based on LEED intensity analysis.

Table 1. Formation conditions of MG on several substrates. (LEED: low-energy electron diffraction; AES: Auger electron spectroscopy; HREELS: high-resolution electron energy-loss spectroscopy; TDS: thermal desorption spectroscopy; SEELFS: surface electron energy-loss fine structure.)

Substrates	Conditions Gases, temperatures, exposures	Experimental techniques	References
TiC(111)	C_2H_4, 1400 K, 200 L	LEED, AES, HREELS	[18]
TaC(100)	C_2H_4, 1400 K, 2000 L	LEED, AES, HREELS	[18]
TaC(111)	C_2H_4, 1100–1500 K, 200 L	LEED, AES, HREELS	[18]
HfC(100)	C_2H_4, 1100–1800 K, 100 000 L	LEED, AES, HREELS	[18,19]
HfC(111)	C_2H_4, 1400 K, 500 L	LEED, AES, HREELS	[18]
WC(0001)	Hydrocarbon, 1800–2000 K	LEED, AES, HREELS	[20]
LaB_6(100)	Segregation	LEED	[21]
Ni(100)	CO, C_2H_4	LEED, AES, UPS	[22, 23]
	CO, 600 K, 90 000 L	SEELFS	[24]
Ni(111)	C_2H_4	LEED, AES	[25]
	Segregation		[26, 27]
Pt(111)	C_3H_6, 1150 K, 13 L	LEED, AES	[28, 29]
	C_6H_6 1100 K, 25 L		
	Segregation		
Ir(100)	C_6H_6, 1600 K, 150 L	AES, TDS	[30]
Ir(111)	C_6H_6, 1600 K, 150 L	AES, TDS	[30]
Pd(100)	Segregation	LEED, AES	[28]
Pd(111)	Segregation	LEED, AES	[28]
Re(1010)	C_6H_6, 1500–1800 K	AES, TDS	[31]
Ru(001)	Segregation	UPS	[32]

2. Experimental set-up

2.1. Growth of thin epitaxial films of graphite and hexagonal boron nitride (h-BN)

In this section, we first describe growth of ultra-thin graphite films on solid surfaces—in particular, one-atomic-layer graphite, which we call 'monolayer graphite' (MG)—and then we mention the growth of h-BN films. Two techniques are known of for achieving the formation of MG so far. The first one is a chemical-vapour-deposition (CVD) technique, in which carbon (C) atoms are supplied from a gas phase. The first experiment was carried out 30 years ago [12, 13]: graphite multilayers grew on various substrates when the substrates were exposed to hydrocarbon gases such as benzene, ethane, and methane, with a suitable reaction temperature maintained. Since the surface dehydrogenation reactivity in the CVD process decreased drastically with the growth of the MG, the growth rates were reduced by factors of 1/10–1/100 by the MG formation, which makes it possible to precisely control the thickness of the MG [14]. That is, the growth of a double atomic layer of graphite (DG) required one or two orders of magnitude more exposure than the growth of MG. Table 1 shows some conditions reported for MG formation on various substrates. On reactive (111) surfaces of Ni and transition metal carbide (TMC), the dehydrogenation occurs at relatively low reaction temperatures as compared to the case for relatively inert surfaces such as Pt and

TMC(100) surfaces. TMC has a rock-salt crystal structure, and hence the (100) surface is a neutral surface composed of metal atoms and C atoms, leading to it being inert as regards surface reactions [15]. In contrast, the TMC(111) surface is a metal-atom-terminated polar surface, and is reactive [16].

The crystalline quality of some MG samples is considerably better than that of kish graphite crystals, which are known to have extremely high crystallographical quality. In comparison with those for the kish graphite crystal, for instance, the LEED spots reflected from MG on TiC(111) were very sharp and the background intensity was quite low. The crystalline quality tends to decrease with decreasing reactivity of the substrate, which suggests that the quality is related to the strength of the interfacial bonds between the MG and the substrate. Films of h-BN of the same quality were grown by means of the CVD technique using borazine ($B_3N_3H_6$) gas [17].

Lastly, we would like to make one comment regarding MG formation: the CVD technique is not useful for all substrates. A typical exception is Si, which forms a stable compound, SiC, by reaction with C.

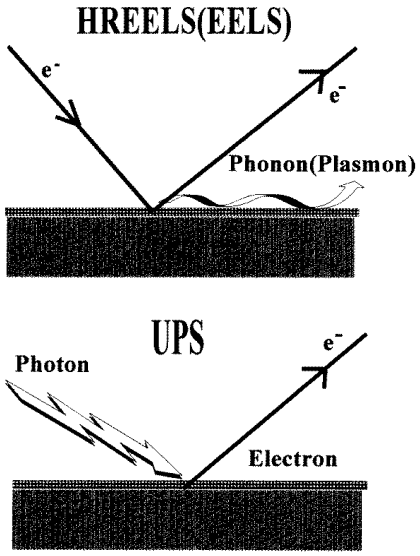

Figure 2. Schematic diagrams of angle-resolved high-resolution electron energy-loss spectroscopy and angle-resolved ultraviolet photoelectron spectroscopy. From the conservation laws of momentum parallel to the plane, the wave vectors of either valence electrons or excited phonons (exited plasmons) are determined.

Another technique for MG formation utilizes the phenomenon of C-atom segregation from the substrates to the surfaces. The segregation in the Ni(111) surface was investigated in detail by Blakely *et al* [22, 25, 26], who demonstrated precise control of the number of surface C atoms by adjusting the annealing temperatures; they found three temperature regions that are correlated with LEED patterns. For the Ni with a C doping level of 0.39 at.%, for instance, in the high-temperature range above ∼1180 K, there is a very dilute carbon phase at the surface, probably with the bulk concentration. The annealing in the middle temperature range brings in an epitaxial MG phase. At the lower temperatures, below ∼1050 K, bulk precipitation occurs. The sharp change from the middle to the lower region indicates adsorption isotherms of the Fowler rather than of the Langmuir type: interactions

within the adsorbate are important, as may be expected for a graphite structure. These transition temperatures became lower as the doping level decreased [26]. Similarly, thin BN films were grown on a specially prepared substrate of stainless steel, whose surface region contains large amounts of B and N atoms [33]. In the subsequent sections, we discuss lattice vibrations and energy band structures of valence electrons in the high-quality films prepared by the CVD technique.

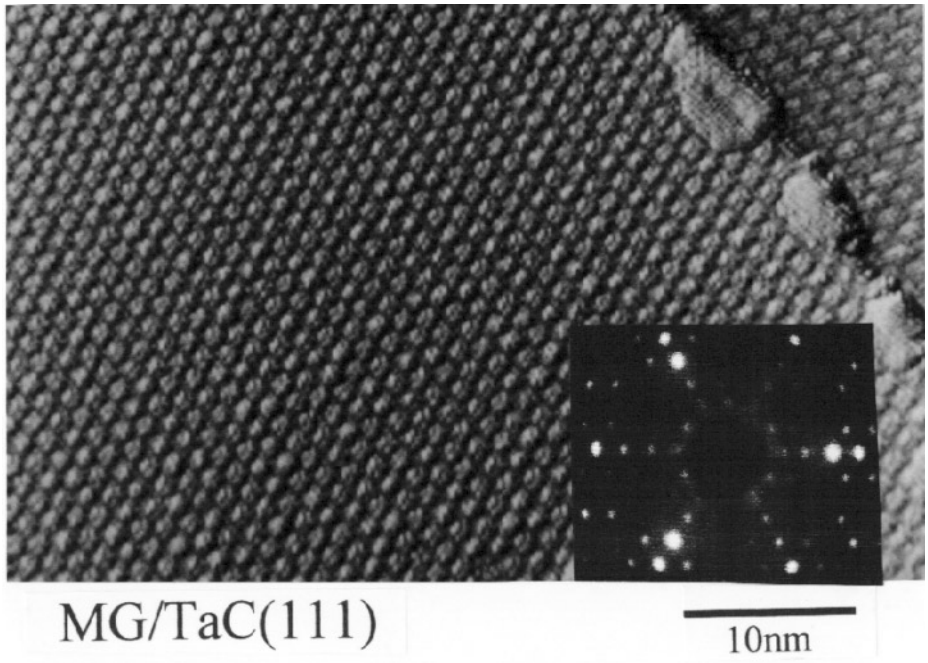

Figure 3. An STM image for MG on TaC(111). The LEED pattern of MG on TaC(111) is also inserted ($E_p = 185$ eV).

2.2. Angle-resolved electron spectroscopy

Figure 2 shows schematic diagrams of the experimental geometry for the angle-resolved electron spectroscopy, HREELS (EELS) and UPS mainly used in this experiment, which provide useful information about energy band structures of valence electrons, and the energy dispersion of phonons (plasmons) in the 2D system. Electron emission from well ordered thin films excited by photons and monochromatized electrons follows the conservation laws of energy and momentum parallel to the surface. That is, the parallel component of the wave vector of either the valence electrons or the exited phonons (the excited plasmons) can be obtained together with the energy. Consequently, angle-resolved spectra determine the energy dispersion curves for either valence electrons or some excitations in the ultra-thin film without ambiguity; these are extremely useful in helping us to understand the electronic and lattice dynamical properties of the 2D system. The direct comparison of the observed curves with calculated ones provides microscopic information, which we discuss in this article.

2.3. Atomic structure of monolayer graphite (MG) and monolayer h-BN

The MG films grown by the CVD technique were observed by scanning tunnelling microscopy (STM), and LEED. Figure 3 is a typical STM image of MG on TaC(111) [34, 35], which exhibits a beautiful incommensurate arrangement; a modulated pattern with two kinds of periodicity, with a large repeat distance ∼1.5 nm and with a short repeat distance ∼0.4 nm, which are much larger than the nearest-neighbour C–C distance (0.14 nm). Hence, the smallest bright points in the STM image do not correspond one C atom, but they are ascribed to the electronic structure modulated with the incommensurate relation. The STM image in figure 3 indicates a uniform large MG area except a small part at a terrace edge, where the second layer started to grow. The LEED pattern (E_p = 185 eV) of MG on TaC(100) is inserted in figure 3, and was in agreement with the 2D Fourier pattern of the STM image. The detailed process of growth of the MG island was observed on Pt(111) until completion of the MG formation by STM [36].

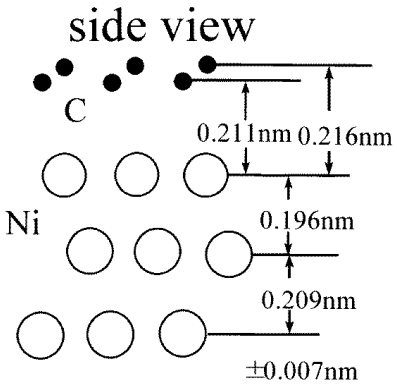

Figure 4. The atomic structure of MG on Ni(111) revealed by a LEED intensity analysis (side view). The error bars for the values in the figure are ±0.007 nm.

The atomic structures of MG on Ni(111) and Pt(111) were analysed by means of a tensor LEED analysis. Figure 4 shows the result at the minimum Pendry's R-factor of 0.23 for commensurate MG on Ni(111) [37]. Two carbon atoms in the unit cell are located either at the on-top site or at the FCC hollow site. In figure 4, the interfacial spacing between the MG and the substrate, 0.21 nm, is much shorter than the interplanar spacing, 0.335 nm, in bulk graphite. The observed short spacing is in accord with the orbital mixing between the π-state of the MG and the d states of the substrates discussed later. No rumpling structure of the MG was detected by the LEED analysis within the experimental accuracy of ±0.007 nm. A similar atomic structure was also found for the monolayer h-BN on Ni(111) with a commensurate 1×1 atomic structure [37]; the N atom of h-BN is situated at the on-top site, and the B atom at the FCC hollow site with the interfacial spacing of ∼0.21 nm.

For incommensurate MG on Pt(111), on the other hand, the large spacing between the MG and the Pt(111) of 0.37 nm was found by using LEED analysis, and an additional carbidic carbon layer was supposed to be inserted at the interface [38]. In general, the MG and the monolayer h-BN films were stable to air exposure; even after air exposure for a few days, we obtained both the same LEED patterns and the same STM images as the original ones observed before air exposure from heat treatments at ∼1100 K in ultra-high

vacuum [34]. The lack of reaction with air is an important property as regards applications in electronic devices.

3. Lattice vibrations (phonons) measured by HREELS

3.1. Surface phonon dispersion of a graphite crystal

High-resolution electron energy-loss spectroscopy (HREELS) is the best experimental technique for determination of surface phonon dispersion curves of a graphite crystal [39, 40].

Although there are the other techniques for detecting phonon signals from these films, the observable modes are strongly restricted; only the vibrational modes at long wavelengths can be measured by optical methods such as infrared absorption spectroscopy and second-harmonic-generation spectroscopy, and He-atom scattering can detect only low-energy (less than 60 meV) phonons; that is, only a small portion of the full phonon dispersion curves of the graphite crystal can be measured [41].

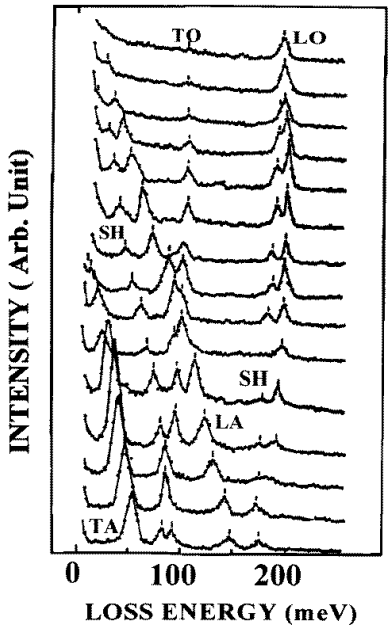

Figure 5. Angle-resolved HREEL spectra obtained from the graphite (0001) surface.

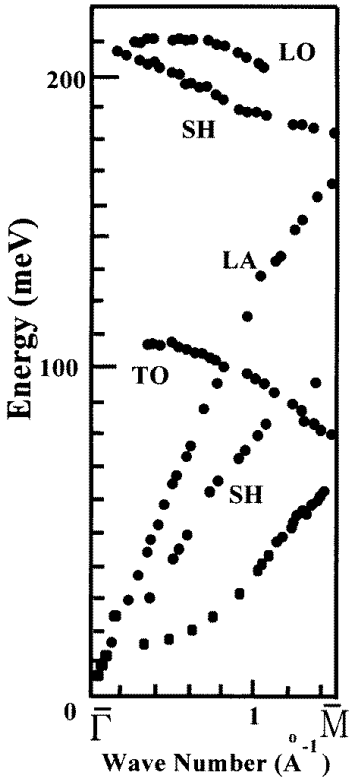

Figure 6. Observed surface phonon dispersion curves over the entire energy region along ΓM of the 2D Brillouin zone of the graphite (0001) surface.

Figure 5 shows a sequence of angle-resolved HREEL spectra measured from graphite (0001). Because a unit cell of the basal plane has two C atoms, we can expect six vibrational modes (three optical and three acoustical ones) for one basal plane. These six branches were

observed in figure 5. Both the loss energies and the intensities changed on changing the incident angle by $\Delta\theta$ away from the specular geometry, keeping the outgoing direction fixed. The wave vectors $q_{\parallel}$ were calculated from the conservation law of momentum parallel to the surface. The plots of the loss energies against $q_{\parallel}$ provide the energy dispersion curves. Figure 6 shows the observed dispersion curves along the ΓM symmetry axis in the 2D Brillouin zone of graphite. The data points are indicated by filled circles. The observed curves connect smoothly to the dispersion curves of the bulk phonons. The electronic broadening of the elastic peak excluded the observation of the phonon branches with $\hbar\omega < 15$ meV and $q_{\parallel} \leqslant 0.2$ Å^{-1}. The extrapolated energies of two high-frequency optical branches agreed with the optical bulk values: 196.9 and 106.9 mV at the Γ point. They are 'in-plane' vibrational modes (LO and SH modes) and an 'out-of-plane' vibrational mode (TO mode). These results indicate that the force field of the intraplanar interaction at the topmost layer is the same as that in the bulk, which is expected from both the slab calculation and a discussion of the structure based on a total energy calculation for one-monolayer graphite crystal; this property originates from the 2D character of the high-frequency (>15 meV) phonons, the vibrational amplitudes of which are strongly localized at each basal plane. For the low-lying phonons, it is theoretically expected that the dispersion curves should agree with the bottom of the bulk phonon continuum. Figure 6 proves that the HREELS experiment can determine the full surface phonon dispersion curves of graphite (0001) over the entire energy region and the entire Brillouin zone.

3.2. Phonon dispersion of MG and monolayer h-BN

Full phonon dispersion curves of the MG on several surfaces were also measured by means of HREELS [18-20, 42–44]. Two typical dispersion curves are depicted in figure 7. The right-hand and left-hand figures represent the dispersion curves of MG on TaC(111) and MG on TaC(100), respectively. Both the LO and TO branches of the MG on TaC(111) shifted to lower values compared with those of the bulk graphite, and, simultaneously, the lattice constant of the MG on the TaC(111), 0.249 ± 0.001 nm, become rather larger than the bulk one, 0.246 nm, which means that the nearest-neighbour C–C bonds weakened. In contrast, all of the observed dispersion curves of the MG on TaC(100) are very close to the bulk ones, and the lattice constant, 0.247 ± 0.001 nm, is very close to the bulk one.

The lattice dynamical calculations of slab crystals based on a force constant (FC) model successfully reproduced the observed curves by adjusting six FCs correlated with either two-body or three-body interactions [42–44]. The calculated results are shown as solid curves in figure 7. In the calculation, we use two stretching FCs related to the nearest and second-nearest C–C bonds and three FCs related to intralayer three-body interaction, and one stretching FC related to the interface bond to fit the experimental curves. Figure 8 represents two typical FCs of the MG selected from the six FCs used for various substrates: one FC (α) relates to a stretching motion of the nearest-neighbour C–C bond, and another FC (γ) is correlated with a restoring force for the out-of-plane motion of the C atom accompanied with a bond-angle change. Ratios of the surface FCs to the bulk ones are plotted against the various substrates as percentages in figure 8. The result in figure 8 clearly shows two MG groups, which we call 'soft MG' and 'normal MG': for the samples of soft MG on the (111) surfaces of TaC, HfC, NbC, ZrC, and TiC, the γ-value decreased to about half of the bulk one; this results from the softening of phonons of longitudinal optical (LO) and transverse optical (TO) modes in the right-hand dispersion curves in figure 7. On the other hand, the γ-value did not change so much for the samples of normal MG on the (100) surfaces of the transition metal carbides (TMCs) and on the WC(0001) surface in figure 8.

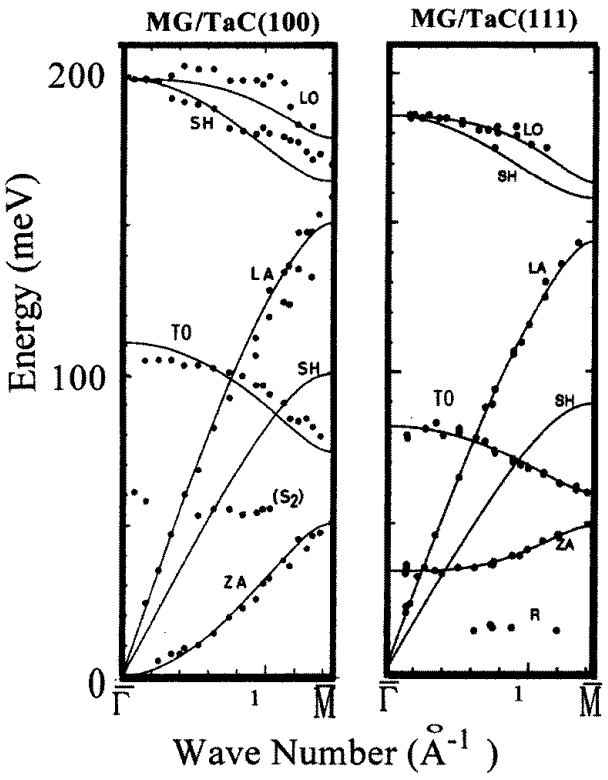

Figure 7. Phonon dispersion curves of MG on a TaC(100) surface and MG on a TaC(111) surface. The solid curves are the calculated ones based on a force constant model.

The soft MG grows on the reactive surfaces.

Another important point is as follows: the two FCs related to the intralayer two-body interactions including α are almost constant for all the MG samples, independently of the substrate, while the three FCs related to the three-body interactions including γ showed a substantial dependence on the type of substrate. These phenomena are strongly correlated with the change in electronic states discussed in the next section.

The observed phonon dispersion of monolayer h-BN on Ni(111) is shown in figure 9 [45]. For comparison, we have depicted the bulk vibrational energies using arrows in figure 9 [46]. The observed energies of LO and TO phonons are somewhat lower than those in bulk crystal, while the vibrational energy of the SH mode with the polarization parallel to the plane agrees with the bulk one. Here, it should be noted that the LO mode is degenerate with the SH mode at the Γ point. In the ionic insulators, in general, these modes should be split by the longitudinal depolarization fields of the LO phonon [47]. As shown by arrows in figure 9, such a split does in fact occur in bulk h-BN. On the other hand, the degeneracy is well known as a characteristic feature of metallic compounds such as TiC, NbC, TaC, and NbN [4], where the conduction electrons in crystals shield the depolarization fields. Consequently, these facts together with figure 9 suggest that the dynamic response of conduction electrons at the Ni surface is the origin of the disappearance of the depolarization fields inside monolayer h-BN. At the same time, the coincidence of the SH energy of the monolayer BN with the bulk one strongly suggests that the intraplanar force fields in the

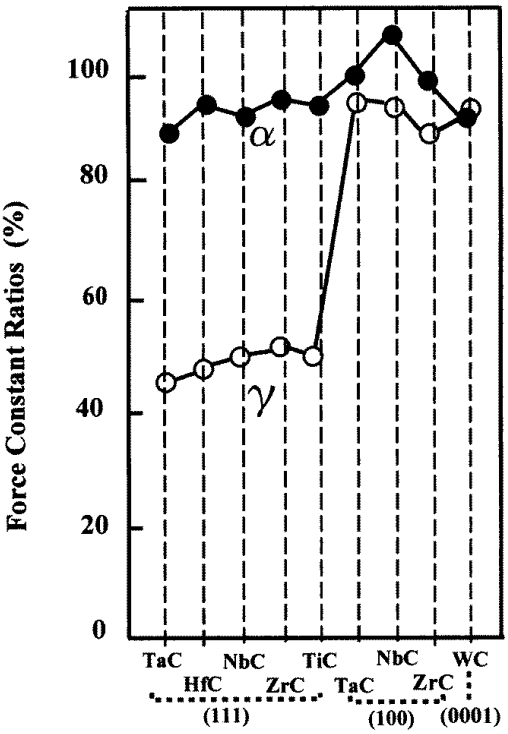

Figure 8. Two force constants (α and γ) selected from six values used to fit the observed dispersion curves of the samples of MG on several substrates. The vertical axis represents the ratios of the force constants of the MG to those of the bulk (in %).

monolayer BN are very close to the bulk one, which is consistent with the electronic band structure of monolayer h-BN discussed in the next section.

4. Electronic structures measured by ARUPS

4.1. Energy bands of MG and double-layer graphite (DG)

As we mentioned above, the samples of soft MG showed the weakening of the intralayer stretching FCs related to the three-body interactions. It is not only the MG but also the alkali metal graphite intercalation compound and alkali-doped C_{60} that show C–C bond weakening through phonon softening and the change in lattice constant. In the latter two systems, the bond weakening is caused by the electron transfer from the intercalants to the carbon allotrope [47]; the electrons from the alkali metal atoms occupy the empty, anti-bonding states of graphite and C_{60}. In contrast to the case of these systems, it is clarified in this section that the physical properties of MG are changed not mainly by the electron transfer from the metal substrate to the graphite layer but by the orbital mixing of the π-states with the d states of the substrate [14, 48–50].

From ARUPS measurements such as those shown in figure 2, the energy dispersion relations of valence electrons in the epitaxial films were determined. Figure 10 shows the results for two typical samples of MG. Open (filled) symbols are data points for soft

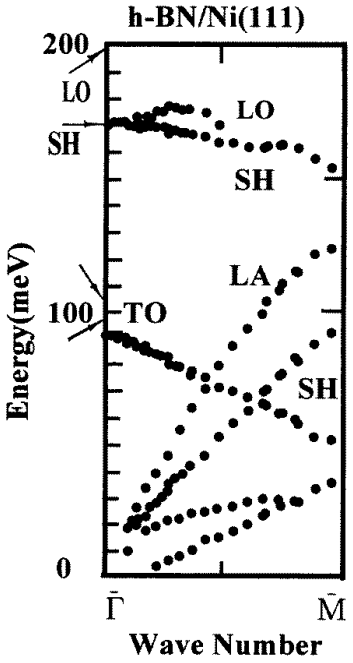

Figure 9. Phonon dispersion curves of the monolayer h-BN on Ni(111).

(normal) MG [14, 50]. In figure 10, the experimental band structure of bulk graphite is also indicated by broken curves for comparison [51]. While the normal MG on the inert (100) surface has an electronic structure similar to that of the bulk graphite, the soft MG on the reactive (111) surface has a different one, of which the characteristics are summarized as follows.

(1) The π-band of the soft MG lies in the binding energy being much deeper than that of the bulk. This is a common feature of soft MG formed on reactive surfaces including TiC(111) and Ni(111) as shown in table 2 [49].

(2) In the bulk graphite, the π-band reaches the Fermi level (E_F) at the K point of the Brillouin zone and connects with the unoccupied π^*-band there [52]. In contrast, the soft MG on TaC(111) has a band gap of 1.3 eV at the K point between the π^*-like conductive band and the π-band, as shown in figure 10.

(3) In contrast to the drastic change of the π-band, the σ-bands agree well with those of the bulk graphite, which is also common for both the soft MG and the normal MG.

(4) As shown in figure 11, a small energy shift of the C 1s XPS peak of MG from the peak of the bulk graphite rules out the possibility of substantial electron transfer from the substrate to the graphite layer. These results clearly indicate that the rigid-band model accompanied with electron transfer is not appropriate for the electronic structure of the MG. Instead, taking into account the fact that the (111) surfaces of the TMCs are terminated with metal atoms [16, 53], it is concluded that the band structure of soft MG on a reactive surface is caused by mixing of the π-states with the d states of the substrate.

The formation of the chemical bond at the interface also leads to the weakening of the in-plane C–C bond in the following way. The mixing of the occupied π-states with

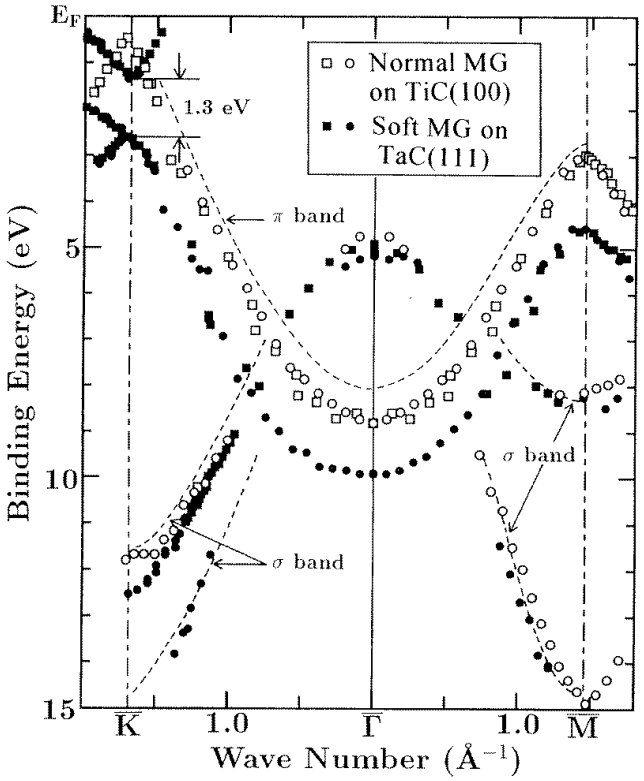

Figure 10. Band structures of soft MG on TiC(100) and normal MG on TaC(111). The dotted lines represent the bulk bands. Squares and circles represent the data points obtained with He I ($h\nu = 21.2$ eV) and He II ($h\nu = 40.8$ eV) resonance lines, respectively.

the unoccupied substrate states reduces the occupation in the π-states. Meanwhile, the occupation of the unoccupied, anti-bonding π^*-states increases due to the mixing with the occupied substrate states, which results in the weakening of the bond in the graphite layer. In other words, the bond weakening is caused by the electron redistribution from the bonding π-states to the anti-bonding π^*-states, whose energies are lowered by the mixing with the substrate state. This process is analogous to the mechanism of C–O bond weakening in CO chemisorbed on transition metal surfaces [55]. The observed orbital mixing was confirmed theoretically for soft MG on TiC(111) and on Ni(111) from *ab initio* energy band calculations [56, 57].

The electron redistribution within the graphite layer also strongly influences the change in the work function. In table 2, we tabulate the observed values (in eV) of the work function of the clean and MG-covered surfaces of several substrates, together with the experimental binding energies of the π-band at the Γ point. The substrates cited, Pt(111), TaC(100), and TiC(100), have relatively inert clean surfaces, on which the MG has shown no substantial C–C bond weakening in the phonon dispersion [42–44], and the π-band has a binding energy rather close to the corresponding value for bulk graphite. As shown in table 2, upon the formation of the MG, the work functions of these inert surfaces become almost the same, being close to the work functions of graphite crystal (4.6 eV), although the work functions of the clean surfaces are quite different from each other, ranging from 4.1 to

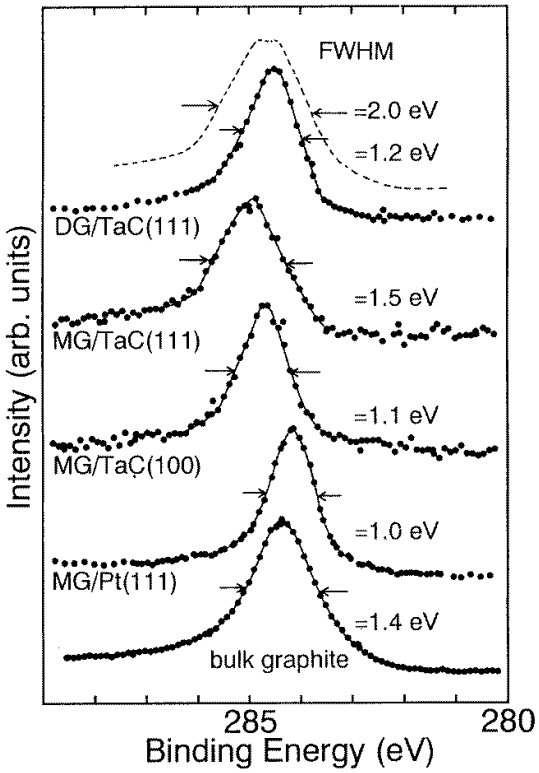

Figure 11. XP spectra of the C 1s peak for various graphite layers.

Table 2. The observed values (in eV) of the binding energy of the π-band at the Γ point and of the work function of the clean and MG-covered surfaces of the substrates. The corresponding values for bulk graphite are also indicated for comparison. An asterisk indicates a substrate on which soft MG is grown.

Substrate	Binding energy (eV) of π-band at Γ	Work function (eV)	
		Clean	Graphite covered
TaC(111)*	9.9	4.7	3.7
	8.4[a]		4.2[a]
TiC(111)*	9.6	4.7	4.2
Ni(111)*	10.3	5.3	3.9
Pd(111)	8.9	5.3	4.3
Pt(111)	8.2	5.8	4.8
TaC(100)	9.0	4.1	4.5
TiC(100)	8.8	4.1	4.5
Graphite	8.1	4.6	

[a] For double-layer graphite.

5.8 eV. These results suggest that in the outermost layers of these systems (i.e. the graphite layers) the charge distribution is similar to that in the graphite crystal, and the work function of the graphite-covered surface is determined mainly by the electronic states in the graphite layer. On the reactive surface, on the other hand, the work function of the MG is fairly

low compared to that of the graphite crystal. Since, in the graphite overlayer, the charge distribution on the interface side should be different from that on the vacuum side due to the chemical bonding at the interface, the observed low work function could be explained as follows: because of the asymmetric charge distribution in the graphite layer, an electric dipole perpendicular to the surface is generated, which reduces the work function.

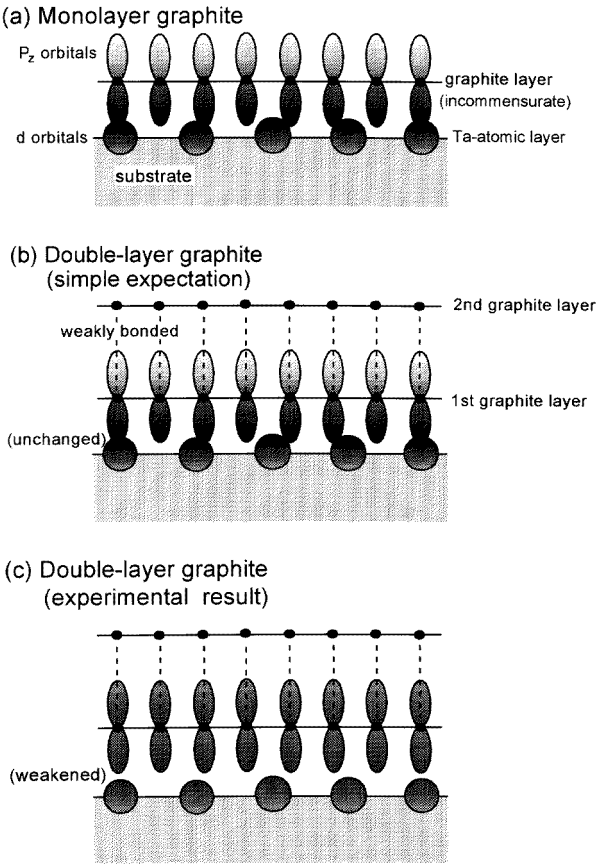

Figure 12. A schematic diagram representing the interaction between the graphite layer and the substrate.

Since graphite is a highly anisotropic material, it may well be supposed that the formation of a second monolayer of graphite would not strongly affect the chemical bonds at the interface between the first monolayer of graphite and the metal substrate; this assumption is, indeed, correct for the graphite overlayer/metal incommensurate system. Figure 11 shows the XP spectra in the C 1s energy region for various graphite overlayers and bulk graphite. In figure 11, as for the spectra of graphite overlayers on TaC substrates, the C 1s peak of the substrate located at ∼283 eV has been subtracted by using the spectra of the clean substrates and, therefore, the overlayer peaks at ∼285 eV are compared straightforwardly to the peaks of bulk graphite and of MG on Pt(111). It should be emphasized that the peak width of double-layer graphite (DG) is smaller than that of the MG formed on the same TaC(111) surface. Before discussing the reason for this phenomenon, we firstly interpret another phenomenon related to it—namely, the fact that normal MG on chemically inert

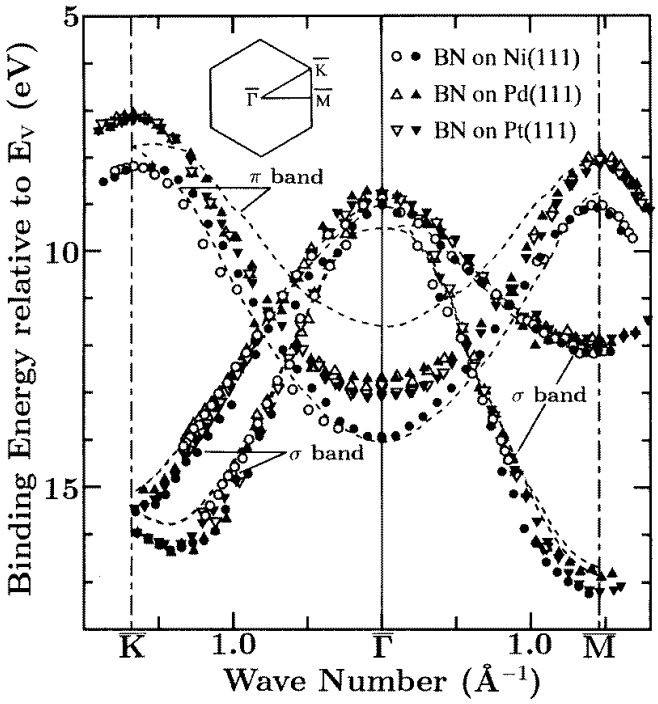

Figure 13. Band structures of monolayer h-BN on the (111) surfaces of Ni, Pd, and Pt. The dotted lines represent the calculated results for h-BN crystal [60].

surfaces such as TaC(100) and Pt(111) has the smallest values (1.0–1.1 eV) of the full width at half-maximum (FWHM) while the largest value, 1.5 eV, is observed for MG on the reactive TaC(111) surface. In normal MG on inert surfaces, the electronic structure is much closer to the bulk one in comparison with that of soft MG on TaC(111); this tendency is observed in the dispersion curves of the π-band, the work function, the lattice constant, and the phonon frequencies. These results indicate that the MG is coupled with the reactive TaC(111) surface more strongly than with the inert surfaces. Figure 12 presents schematic diagrams of chemical bonds of the overlayer with the substrate. As shown in figure 12(a), the positions of the neighbouring carbon atoms in the overlayer are not identical with each other because of the incommensurate relationship with the substrate. Therefore, the many different bonds due to the relatively strong mixing of the states produce different electron distributions around the carbon atoms, which involves the differences in the initial-state energy (chemical shift) and the screening effects for the core hole (relaxation shift or lifetime broadening). This is presumably the origin of the broad peak of the MG on TaC(111). The broad peak of the graphite crystal in figure 11 is ascribed to the poor crystallinity due to defects such as incorrect stacking of the basal planes, corrugation, and steps, because we saw ring-like diffraction spots with a high background in the LEED pattern of the graphite crystal.

Next, the peak width of the DG in figure 11 is discussed. Because of the large mean free path of the x-ray photoelectrons, the spectrum of the DG is composed of signals not only from the second layer of the graphite but also from the first layer. If the formation of the second graphite layer did not strongly influence the interfacial bonds between the first

layer and the substrate as illustrated in figure 12(b), the spectrum of the DG would be very broad, like the broken curve in figure 11; it was calculated by superposing the spectrum of the bulk graphite on that of the MG on TaC(111). However, the result in figure 11 shows that the C 1s peak of the graphite overlayer becomes narrow by the time the of the second-layer growth. This fact strongly suggests that the formation of the second layer causes all of the carbon atoms in the two layers to have similar states. In addition to this, the observed band structure of the graphite film becomes very similar to that of bulk graphite with the increase in the thickness from one to two layers, and the lattice constant of the DG (0.247 ± 0.001 nm) estimated from the LEED pattern is closer to the bulk one (0.246 nm) than that of MG (0.249 ± 0.001 nm). These results demonstrate that the physical properties of the graphite film become similar to those of the corresponding bulk with increase in the thickness. Therefore, we conclude that the bulk-like weak interlayer bonds are produced between the two basal planes in the DG, and the strengths of the interfacial bonds are reduced, as is illustrated in figure 12(c). In other words, it could be inferred that the interplanar bonds with a commensurate relationship contribute to the cohesive energy more substantially than those with the an incommensurate relationship. This result was consistent with the observed difference in dispersion curves between MG and DG [50].

Recently, ARUPS experiments clarified that the intercalation of the alkali metal atoms between MG and the Ni(111) surface causes the dilation of the interlayer distance, which makes the interfacial bonds weaken [54]. As a consequence, the band structure of the MG becomes similar to the bulk one with increasing radius of the intercalants. This conclusion is in good accord with the work-function change involved upon intercalation, which suggests that the absorbed alkali metal atoms are strongly bonded to the Ni substrate but not to the graphite layer.

4.2. Energy bands of monolayer h-BN

Figure 13 shows the dispersion relations of valence electrons of monolayer h-BN grown on the (111) surfaces of Ni, Pd, and Pt [58, 59]. In figure 13, the valence band structures for the BN films on these substrates agree well with each other; this is in contrast to the case for MG discussed above. The results suggest that the interfacial bond between the BN film and the substrate is weaker than in the case of MG on the same substrates. This difference as regards the interfacial bond (i.e. the mixing of the states) between monolayer h-BN and MG arises from the fact that while graphite is a semi-metal, BN is an insulator with a band gap of $\sim$6 eV. The absence of electronic states near E_F results in there being no substantial mixing in the present system. As shown in figure 13, the π-band of the h-BN films on Ni(111) has a binding energy deeper by $\sim$1 eV than those of films on the other two substrates. As for the shape of the dispersion curves, however, the π-bands on the three substrates are quite similar to each other—this is unlike the case for MG; the deformation of the dispersion curve depending on the substrate has not occurred. The difference in band structure between the h-BN films on Ni(111) and those on the other substrates, therefore, lies in the rigid energy shifts of the π-band. In figure 13, the theoretical band structure of bulk h-BN calculated by Catellani *et al* [60] is also indicated by broken lines for comparison, where the entire theoretical dispersion curves were shifted rigidly to fit the experimental data. Taking into account the fact that the π-band in bulk BN splits into two due to the interlayer interaction between the neighbouring basal planes in a unit cell, the correspondence between the experimental band structure for monolayer h-BN and the theoretical one for the bulk is fairly good.

5. Dispersion curves of 2D plasmons of MG measured by EELS

Two-dimensional (2D) plasmons, whose charge fluctuations are strongly localized at a monolayer, have been discussed theoretically for a long time [61–65]. Near the Γ point, the 2D plasmons due to intrasurface and intersurface band transitions have the following peculiar dispersion relations, respectively [65]:

$$\omega_p^2 = 4\pi e^2 N q/\{m^*(1+\varepsilon)\} \tag{1}$$

and

$$\omega_p^2 = \beta + \eta q \tag{2}$$

where N is the electron density per unit area, m^* the effective electron mass, and ε the dielectric constant of the substrate. In equation (2), β consists of two parts; one is for the transition energy between the occupied and unoccupied energy bands and the other for a depolarization term. Since ηq expresses the energy of interaction between the induced electric dipoles, it becomes positive (negative) for polarization parallel (perpendicular) to the surface. In contrast to the theoretical progress on the 2D plasmons, only a few experimental data have been reported so far [66–68], because it was difficult to prepare an excellent 2D system in which a large number of electrons are confined.

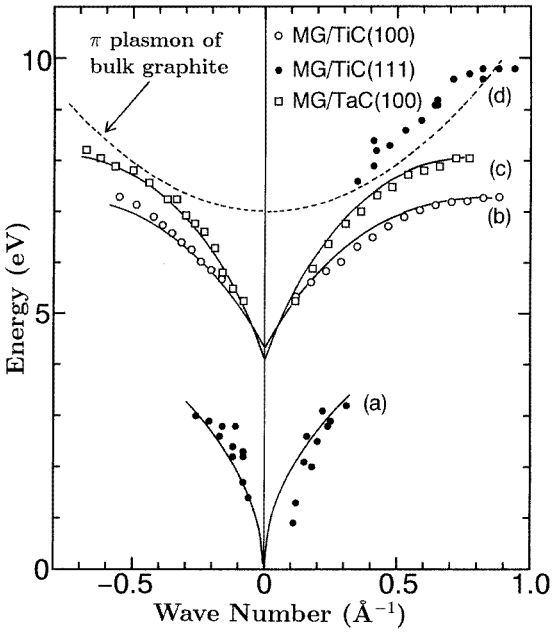

Figure 14. Dispersion relations of 2D plasmons excited in normal MG on TiC(100) and TaC(100), and in soft MG on TiC(111).

As is manifested in figure 10, the observed electronic states of the MG-on-metal systems are strongly localized within the graphite layer and/or at the interface; the dispersion curves measured with He I agree perfectly with those measured with He II, indicating the absence of energy dispersion perpendicular to the plane. Owing to the strong localization of the electronic states, the plasmons observed in the present systems showed dispersion relations characteristic for the 2D system.

Similarly to the case of phonons, the dispersion curves of plasmons were determined from angle-resolved EELS by using two conservation laws. Figure 14 shows some experimental dispersion curves of the loss peaks in the AREEL spectra for soft MG on TiC(111), and normal MG on TaC(100) and TiC(100). The data points on the right-hand (left-hand) side of the Γ point were obtained at scattering angles lower (higher) than the angle corresponding to zero wave vector. All of the observed curves are very different from those of the bulk graphite and those of the substrate. In the bulk graphite, two branches are known. One is located above 25 eV, which is attributed as indicating the plasmon of the π- and σ-electrons. Another one is located in the energy region above 7.0 eV, which is assigned as being the plasmon of the π-electron. The π-plasmon disperses parabolically as shown by the dotted curve in figure 14, which is a characteristic feature of the 3D plasmons [69]. In figure 14, the branch (b) is very similar to branch (c) observed for soft MG on a different substrate, which suggests that these branches are related mainly to the electronic states in the MG but not to those of the substrates. For the following reasons, these branches are assigned as indicating the 2D plasmons due to transitions from the π-band to the π^*-band. Firstly, the peak intensity decreases as the scattering angle departs from the specular direction, which signifies that the scattering mechanism is a long-range dipole scattering. Secondly, near the Γ point, the experimental dispersion relations of branches (b) and (c) agree with the theoretical one expressed by equation (2). Lastly, the energies of these branches are close to that of the π-to-π^* volume plasmon in the graphite crystal shown by the dotted parabolic curve in figure 14.

Compared to AREEL spectra for normal MG on inert TMC(100), those for soft MG on TiC(111) differ drastically owing to the chemical bonding at the interface. We observed two large loss peaks, whose dispersion curves are plotted with filled circles. The low-energy branch (a) is proportional to $q^{1/2}$, a characteristic feature of the plasmons of 2D conduction electrons. From the phenomenological equation for the branch (a), $\hbar\omega = 6.0q^{1/2}$, together with equation (1), the density of the conduction electrons is estimated to be $N = 1.3 \times 10^{15} \times (m^*/m)$ cm^{-2}, which is much higher than the carrier density (electron and holes) in bulk graphite ($\sim 10^{11}$ cm^{-2}). The electron density estimated on the basis of the band structures observed via ARUPS is 7.4×10^{14} cm^{-2} [70], in good accord with the observed one. Hence, it is concluded that the mixing of the states at the interface produces new conduction bands containing 2D electrons with the high density of $\sim 10^{15}$ cm^{-2}, which is the origin for the observed intrasurface band plasmon.

6. Conclusions

Recent angle-resolved electron spectroscopy revealed the phonon dispersion, electronic band structures, and 2D plasmons of MG, DG and monolayer h-BN on solid surfaces. We summarize some conclusions reached in this article as follows.

(1) On the basis of the observed phonon dispersion, the MG was classified into two groups: normal MG and soft MG. The soft MG was characterized by a large reduction in the FCs related to the intralayer three-body interactions, expansion of the nearest-neighbour C–C distance, modification of the π-branch, a relatively low work function, and intraband 2D plasmons with high carrier density. All of these phenomena stem from the interfacial mixing of the π-state and the d state of the substrate. All of the samples of soft MG were grown on relatively reactive surfaces such as Ni and TMC(111) surfaces.

(2) On the other hand, all of the observed properties of normal MG are very close to the bulk ones. Normal MG grows on relatively inert surfaces such as Pt(111) and TMC(100).

(3) In contrast to the π-band, the σ-bands of both soft MG and normal MG are almost unchanged from the bulk ones, and, in addition, the two stretching FCs related to the two-body interactions are also close to the bulk ones. Hence, the facts strongly suggest that the σ-bonds between the nearest C–C interactions are correlated with the two FCs related to the two-body interactions.

(4) As compared to that of the MG, the interfacial interaction between the monolayer h-BN and the substrate is weak. This is because the h-BN film is an insulator with a large band gap, resulting in no substantial mixing of the π-state with the d state of the substrate.

References

[1] Pauling L 1960 *The Nature of Chemical Bonds* (Ithaca, NY: Cornell University Press)
[2] Kinoshita K 1988 *Carbon* (Toronto: Wiley)
[3] Niklow R, Wakabayashi N and Smith H G 1972 *Phys. Rev.* B **5** 4951
[4] Bilz B and Kress W 1979 *Phonon Dispersion Relations in Insulators* (Berlin: Springer)
[5] Iijima S 1991 *Nature* **354** 56
[6] Rubio A, Corkill J L and Cohen M L 1994 *Phys. Rev.* B **49** 5081
[7] Ueda R 1991 *Prog. Mater. Sci.* **35** 58
[8] Ishizawa Y, Koizumi M, Oshima C and Otani S 1987 *J. Physique Coll.* **48** C6
[9] Fujita D and Honma T 1992 *Surf. Interface Anal.* **19** 430
[10] Itakura A, Tosa M and Yoshihara K 1994 *J. Vac. Soc. Japan* **37** 793
[11] Koma A 1992 *Surf. Sci.* **267** 29
[12] Hess W M and Ban L L 1966 *Proc. 6th Int. Congr. on Electron Microscopy (Kyoto)* vol 1, p 569
[13] Karu A E and Beer M 1966 *J. Appl. Phys.* **37** 2179
[14] Nagashima A 1995 *PhD Thesis* Waseda University
[15] Oshima C, Aono M, Tanaka T, Zaima S and Shibata Y 1981 *Surf. Sci.* **102** 312
[16] Oshima C, Aono M, Zaima S, Shibata Y and Kawai S 1981 *J. Less-Common Met.* **82** 69
[17] Simon R J and Trenary M 1990 *J. Electron Spectrosc. Relat. Phenom.* **54+55** 717
[18] Aizawa T 1990 *J. Surf. Sci. Soc.* **11** 398 (in Japanese)
[19] Aizawa T, Souda R, Otani S, Ishizawa Y and Oshima C 1990 *Phys. Rev. Lett.* **64** 768
[20] Aizawa T 1995 private communications
[21] Oshima C, Bannai E, Tanaka T and Kawai S 1977 *Japan. J. Appl. Phys.* **16** 965
[22] Isett L C and Blakely J M 1976 *Surf. Sci.* **58** 397
[23] McConville C F, Woodruff D P and Kevan S D 1985 *Surf. Sci.* **161** 373
[24] Papagno L and Caputi L S 1984 *Phys. Rev.* B **29** 1483
[25] Eizenberg M and Blakely J M 1979 *Surf. Sci.* **82** 228
[26] Blakely J M and Shelton J C 1975 *Surface Physics of Crystalline Materials* ed J M Blakely (New York: Academic)
[27] Rosei R, De Crescenzi M, Sette F, Quaresima C, Savoia A and Perfetti P 1983 *Phys. Rev.* B **28** 1161
[28] Hamilton J C and Blakely J M 1980 *Surf. Sci.* **91** 199
[29] Hu Zi-pu, Ogletree D F and Somorjai M A 1987 *Surf. Sci.* **180** 433
[30] Kholin A, Rut'kov E V and Tontegode A Ya 1985 *Sov. Phys.–Solid State* **27** 155
[31] Gall N R, Mikhallov S N, Rut'kov E V and Tontegode A Ya 1985 *Sov. Phys.–Solid State* **27** 1410
[32] Himpsel F J, Christmann K, Heimann P, Eastman D E and Feibelman P J 1982 *Surf. Sci.* **115** L159
[33] Yoshihara Y, Tosa M and Nii K 1985 *J. Vac. Sci. Technol.* A **3** 1804.
[34] Itoh H, Ichinokawa T, Ichinose T, Oshima C and Aizawa T 1991 *Surf. Sci. Lett.* **254** 437
[35] Oshima C, Itoh H, Ichinokawa T, Aizawa T, Souda R, Otani S and Ishizawa Y 1992 *Ordering at Surfaces and Interface* ed A Yoshimori (Berlin: Springer) p 13
[36] Land T A, Michely T, Behm R J, Hemminger J C and Comsa G 1992 *Surf. Sci.* **264** 261
[37] Gamou Y, Nagashima A, Wakabayashi M, Terai M and Oshima C 1996 *Surf. Sci.* at press
[38] Hu Zi-pu, Ogletree D F, Van Hove M A and Somorjai G A 1987 *Surf. Sci.* **180** 433
[39] Wilkes J L, Palmer R E and Willis R F 1987 *J. Electron Spectrosc. Relat. Phenom.* **44** 355
[40] Oshima C, Aizawa T, Souda R, Ishizawa Y and Sumiyoshi Y 1988 *Solid State Commun.* **65** 1601
[41] Benedek G, Brusdeylins G, Heimlich C, Toennis J P and Valbusa U 1986 *Surf. Sci.* **178** 545
[42] Aizawa T, Souda R, Otani S, Ishizawa Y and Oshima C 1990 *Phys. Rev.* B **42** 11 469

[43] Aizawa T, Souda R, Otani S, Ishizawa Y, Hirano H, Yamada T, Tanaka K and Oshima C 1990 *Surf. Sci.* **237** 1943
[44] Aizawa T, Hwang Y, Hayami W, Souda R, Otani S and Ishizawa Y 1990 *Surf. Sci.* **260** 311
[45] Rokuta E, Hasegawa Y, Suzuki K and Oshima C 1996 unpublished
[46] Geick R, Perry C H and Rupprecht G 1952 *Phys. Rev.* **146** 543
[47] Chan T C, Kamitakahara W A, Ho K M and Eklund P C 1987 *Phys. Rev. Lett.* **58** 1528
[48] Nagashima A, Nuka K, Itou H, Ichinokawa T, Oshima C and Otani S 1993 *Surf. Sci.* **291** 93
[49] Nagashima A, Nuka K, Sato K, Itou H, Ichinokawa T, Oshima C and Otani S 1993 *Surf. Sci.* **287/288** 609
[50] Nagashima A, Itou H, Ichinokawa T, Oshima C and Otani S 1994 *Phys. Rev.* B **50** 4756
[51] Takahashi T, Tokailin H and Sagawa T 1985 *Phys. Rev.* B **32** 8317
[52] Tatar R C and Rabii S 1982 *Phys. Rev.* B **25** 4126
[53] Hayami W, Souda R, Aizawa T, Otani S and Ishizawa Y 1993 *Phys. Rev.* B **47** 13 752
[54] Nagashima A, Tejima N and Oshima C 1994 *Phys. Rev.* B **50** 1787
[55] Blyholder G 1964 *J. Phys. Chem.* **68** 2772
[56] Kobayashi K and Tsukada M 1994 *Phys. Rev.* B **49** 7660
[57] Souzu Y and Tsukada M 1995 *Surf. Sci.* **326** 42
[58] Nagashima A, Tejima N, Gamou Y, Kawai T and Oshima C 1995 *Phys. Rev.* B **51** 4606
[59] Nagashima A, Tejima N, Gamou Y, Kawai T and Oshima C 1995 *Phys. Rev. Lett.* **75** 3918
[60] Catellani A, Postermak M, Baldereschi A, Jansen H J F and Freeman A J 1987 *Phys. Rev.* B **36** 6105
[61] Stern F 1967 *Phys. Rev. Lett.* **18** 546
[62] Newns D M 1972 *Phys. Lett.* **38A** 341
[63] Kuramoto Y and Kamimura H 1974 *J. Phys. Soc. Japan* **37** 716
[64] Nakayama M, Kato T and Ohtomi K 1984 *Solid State Commun.* **50** 409
[65] Grimes C C and Adams G 1976 *Phys. Rev. Lett.* **36** 145
[66] Allen S J Jr, Tsui D C and Logan R A 1977 *Phys. Rev. Lett.* **38** 80
[67] Aruga T, Tochihara H and Murata Y 1984 *Phys. Rev. Lett.* **53** 372
[68] Nagashima A, Nuka K, Itoh H, Ichinokawa T, Oshima C, Ishizawa Y and Otani S 1992 *Solid State Commun.* **83** 581
[69] Venghaus H 1974 *Phys. Status Solidi* b **66** 145
[70] Nagashima A, Nuka K, Tejima N, Otani S and Oshima C 1994 *Advanced Materials '93; Superconductors, Surface and Superlattices* ed H Sakai *et al* (Amsterdam: Elsevier Science) p 107